Materials Horizons

ROYAL SOCIETY OF CHEMISTRY

COMMUNICATION

View Article Online
View Journal | View Issue

Cite this: *Mater. Horiz.*, 2025, **12**, 10760

Received 30th June 2025,
Accepted 22nd August 2025

DOI: 10.1039/d5mh01248a

rsc.li/materials-horizons

A chessboard-like photothermoelectric cement cell: a new design for scalable and high efficiency solar energy conversion

Mohamad Barzegar,* [a] Guido Goracci,[a] Pavel Martauz[b] and Jorge S. Dolado*[ac]

wA scalable, low-cost photothermoelectric (PTE) cell using cementitious blocks in a chessboard-like design with varying solar absorbance achieves up to 1.81 × 10^6 μJ m^{-2} and ~10 mV K^{-1} Seebeck coefficient—among the highest for PTE materials. This highlights the potential of engineered cement for efficient solar energy harvesting in smart, sustainable infrastructure.

New concepts

This study introduces the first chessboard-like photothermoelectric (PTE) cement cell—a low-cost, scalable system that exploits contrasting optical properties in cement composites to generate horizontal temperature gradients under sunlight. Unlike conventional ionic thermoelectric (iTE) systems that require complex materials and face challenges like leakage or high cost, our cement-based PTE cell uses abundant materials—geopolymer and white cement combined with copper slag aggregate—to drive ionic charge separation *via* the Soret effect. The unique geometry, mimicking a chessboard of alternating solar absorbers and reflectors, enables directional ion migration and stable voltage generation in real-world conditions. This approach overcomes the longstanding limitation of inefficient vertical gradients in cement-based TE systems and delivers a record-high Seebeck coefficient of 9.9 mV K^{-1}—surpassing all previously reported values for cementitious materials. Moreover, our work pioneers the concept of self-recharging PTE cement, leveraging ambient humidity to restore functionality after drying, thus enabling continuous operation without liquid electrolytes. By combining material engineering, geometric optimization, and field-tested environmental integration, this concept redefines how solar heat can be harvested within construction materials, offering a disruptive new strategy for embedding renewable energy functions directly into urban infrastructure.

1. Introduction

Modern cities are characterized by high energy demands, which contribute to environmental issues such as increased greenhouse gas emissions, urban heat islands, and reliance on fossil fuels.[1–3] Addressing these challenges requires transformative solutions that convert urban areas into active energy generators. Integrating renewable sources into urban infrastructure is a key challenge as global energy transitions progress. Urban surfaces absorb substantial amounts of solar irradiation, and converting this energy into usable electricity is essential for the next generation of smart grids, which require complementary and sustainable energy sources.[4,5]

Photothermoelectric (PTE) technology plays a crucial role in this context by converting solar energy first into heat and then into electricity. Various PTE technologies have been explored,[6,7] and conventional thermoelectric (TE) materials typically require high temperatures (>500 K) for optimal performance.[8] However, ionic thermoelectric (iTE) systems, which operate efficiently at lower temperatures and generate higher thermal voltages in the millivolt per Kelvin (mV K^{-1}) range, offer promising alternatives.[9,10] These systems utilize the Soret effect, where ion migration across a thermal gradient leads to charge accumulation and an electric field.[11] Nevertheless, challenges such as scalability, cost, toxicity, and seamless integration into current urban architecture have hindered their widespread adoption.[12,13]

Cement and concrete, as dominant materials in urban infrastructure, present a significant opportunity for energy harvesting because of their vast surface coverage.[14] Cementitious materials, previously considered electronic TE materials, have recently demonstrated iTE effects,[15–20] making them potential candidates for ambient energy harvesting. Previous studies have shown that the iTE effect in cement-based materials can be leveraged for temperature sensing,[21] with pore solution ions enhancing thermovoltage generation.[21–24]

However, a fundamental unsolved challenge in cement-based TE materials is the small temperature difference (ΔT), as the thermal gradient is generated vertically, which limits

[a] *Centro de Física de Materiales, CSIC-UPV/EHU, Paseo Manuel de Lardizábal 5, 20018 Donostia-San Sebastián, Spain. E-mail: Mohamad.barzegar@ehu.eus, j.dolado@ehu.eus*
[b] *Považská Cementáreň Cement Plant (PCLA), Ulica Janka Kráľa, 01863 Ladce, Slovakia*
[c] *Donostia International Physics Center (DIPC), Paseo Manuel de Lardizabal 4, 20018 Donostia-San Sebastián, Spain*

their efficiency.[25,26] To address this challenge, we propose the development of the first photothermoelectric cement composite capable of generating a horizontal thermal gradient. By incorporating geopolymer cement, which has demonstrated potential as a thermoelectric material, with copper slag aggregate, we enhance both the thermoelectric performance and solar energy absorption. Copper slag acts as an efficient solar energy absorber, contributing to the heating of the hot part of the cell while also improving the overall thermoelectric efficiency. Additionally, white cement, which naturally has high reflectance, is used to form the cool part of the cell. This novel composite design utilizes the optical properties of different cement types to induce controlled temperature variations, akin to a chessboard pattern, thereby significantly enhancing the thermoelectric performance.

In our study, we demonstrated the effectiveness of this method for the first time through real-world outdoor measurements, where the developed PTE cell exhibited a high Seebeck coefficient of 9.9 mV K^{-1} for two connected cells, the highest reported value for cement-based TE materials.[27] Furthermore, the scalability and cost-effectiveness of this system make it a viable solution for energy harvesting applications. Unlike conventional iTE materials, which are prone to leakage and evaporation, our cement-based PTE cells demonstrate self-recharging capabilities by absorbing ambient humidity after drying, allowing continuous operation.[28] This active construction material can be seamlessly integrated into current urban designs, from pavements and facades to rooftops, enabling cities to transition from energy consumers to energy producers. By investigating the collective behaviour of interconnected PTE cells under varying solar irradiation levels, this study contributes to the advancement of efficient TE systems for sustainable urban energy applications.

2. Experimental methods

2.1. Materials and sample preparation

For the present study, industrial geopolymer-based hybrid cement (GHC) sourced from Považská cementáreň a.s. served as the cement paste for fabricating distinct sections of the TE cells, demarcated by their light-absorption characteristics. The hybrid cement composition included 90% geopolymer and 10% ordinary Portland cement (OPC). The part designed to exhibit higher light absorbance is referred to as the ''black part''. To augment the iTE behaviour of this part, 75 wt% copper slag aggregate from the Považská company was deliberately included. In contrast, the counterpart section with a higher light reflectance was created by employing white cement BL I 52.5 R from Cementos Cruz (Spain). Table 1 presents the chemical compositions of the GHC, white cement (BLWC), and CS. The chemical composition of the raw materials was analysed *via* X-ray fluorescence (XRF). To prepare the samples, each powder was fused in an induction microfurnace with Spectromelt A12 flux from Merck (ref. no. 11802) at an approximate 20 : 1 ratio, forming borated glass beads. These beads were then examined under a vacuum atmosphere *via* a PANalytical AXIOS sequential wavelength dispersive X-ray fluorescence (WDXRF) spectrometer equipped with an Rh tube. Additionally, the loss on ignition (LOI) was determined by heating a portion of each sample to 1050 °C for one hour in a muffle furnace.

A uniform protocol for sample preparation was adopted for both the black and white sections. Initially, a Hei-TORQUE 200 Overhead Stirrer was employed to facilitate dry mixing of the aggregates and cement at a speed of 300 rpm, ensuring their thorough integration. Subsequently, distilled water was meticulously introduced into the mixture, which was then mixed at 700 rpm for 1.5 minutes. Following a brief interval of 1 min, the mixing procedure was repeated to guarantee homogeneity.

The subsequent step involved casting samples into sealed cubic silicon moulds, with a plastic barrier positioned at the mould centre. Each sample was $8 \times 2 \times 0.7$ cm^3 in size, with each component having a size of $4 \times 2 \times 0.7$ cm^3. The plastic barrier effectively segregated the distinct sections without engendering any undesirable mixing. After 5 min, the plastic barrier was removed, allowing unimpeded pore solution network continuity in both sections. After 24 h, the samples were demoulded and subjected to a 28-day curing process by immersion in a distilled water environment. The same water-to-cement ratio (w/c) of 0.6 was used for all the components.

To increase the repeatability of the measurements and minimize variations in the starting conditions caused by slight inhomogeneities in the pore structure, the samples underwent a specific pretreatment before the Seebeck tests. After the curing period of 28 days, the samples were dried overnight at 50 °C and subsequently stored in an environment with 75% RH for one night.

The infrared emissivity of the samples was measured *via* a 12° gold-coated integrating sphere connected to a Jasco 6300 spectrometer positioned in a downwards-facing setup with a mercury–cadmium–telluride (MCT) detector (PIKE Technologies). All the measurements were carried out at room temperature. To minimize errors from background noise and lamp intensity variations, background spectra were recorded just before each sample measurement. Emissivity values were

Table 1 Chemical compositions of the different parts of the PTE cell

	SiO_2	Al_2O_3	Fe_2O_3	MnO	MgO	CaO	Na_2O	K_2O	TiO_2	P_2O_5	SO_3	Loss on ignition (%)
GHC	35.86	13.51	4.63	0.06	1.79	23.93	3.36	1.97	0.61	0.21	5.02	5.51
BLWC	20.74	3.76	0.16	LD	0.52	62.94	LD	0.64	0.23	0.05	3.26	4.06
CS	22.01	8.86	50.87	0.80	1.48	7.90	0.43	0.24	0.18	0.54	0.25	2.63

calculated as the average of five independent measurements taken for each sample.[4,5]

To improve the energy output of cement-based PTE cells, several modifications have been made to the sample design, electrode configuration, and conductivity enhancement. The sample preparation followed a uniform protocol previously described. Specifically, to reduce the distance between the electrodes, moulds with 50% reduced size were used, while all other aspects of the preparation remained unchanged.

To investigate the effects of the modifications on the internal resistance and energy output of the PTE cells, three key adjustments were made:

1. *Sample size optimization*: the sample dimensions were modified to $2 \times 0.7 \times 4$ cm^3 to reduce the distance between the electrodes, potentially improving the energy harvesting efficiency.

2. *Contact resistance reduction*: copper electrodes were replaced with soldered wires connected to silver paint electrodes to minimize contact resistance between the electrode and the sample surface.

3. *Conductivity improvement*: the ionic conductivity of the samples was enhanced by submerging them in a 3.5 wt% NaCl solution (seawater concentration). The samples were dried at 50 °C overnight after 28 days of curing and then submerged in saline solution for 1 hour. Afterwards, the samples were removed and allowed to rest for 24 hours before measurement.

The resistance and conductivity were measured using a 2-probe measurement setup and a KEITHLEY 2100 6 $\frac{1}{2}$ Digit Multimeter.

Seebeck measurement

Two types of Seebeck measurements were conducted in this study: indoor measurements under controlled conditions and outdoor measurements in real-world environments. The test setups for the outdoor and indoor measurements are shown in Fig. 1a and b.

During the laboratory measurements, a single PTE cell composed of black and white segments was used to investigate the dependence of the PTE voltage on the solar power level. Diverse light irradiation conditions were implemented by adjusting the vertical distance between the PTE cell and a 500 W halogen light source. Two, four, and six samples were subsequently connected in series and placed under 850 W m^{-2} to assess the feasibility of scaling up TE energy conversion *via* a chessboard arrangement.

The moisture reabsorption ability of the PTE cells post-drying was assessed *via* water contact angle (WCA) measurements using an optical tensiometer (UI-122XLE-M, IDS, Germany). A 2 μL distilled water droplet was deposited on each sample surface and allowed to equilibrate before imaging. WCA values were calculated using the ellipse-fitting method in SCA20 software. To account for surface heterogeneity, measurements were taken at three distinct points per sample and averaged to quantify surface wettability. However, the rechargeability of the PTE cement composite depends not only on its capacity to absorb moisture but also on its ability to regenerate the same PTE voltage after drying. The samples were dried at 50 °C overnight and then stored for 8 hours in a humidity chamber with a relative humidity (RH) of 50%. After this treatment, the samples were tested under light irradiation to assess their potential to restore the same voltage after drying.

The outdoor measurements were obtained on the rooftop of the Centro de Física de Materiales in San Sebastian, Spain. The TE response of two samples connected in series was monitored over three sunny days during August 2024 (27/08/2024 to 29/08/2024). Weather conditions, including the RH and ambient

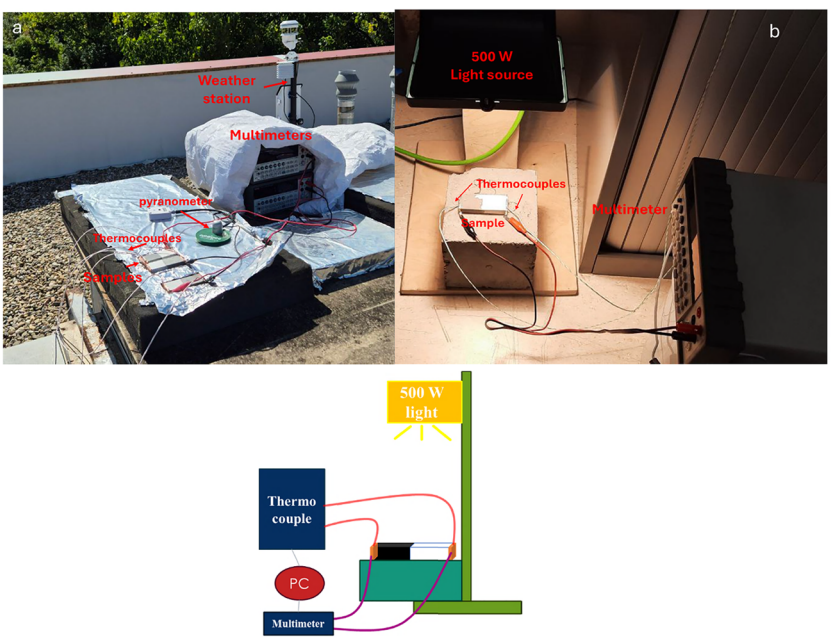

Fig. 1 (a) Setup for the outdoor PTE test. (b) Setup for the indoor PTE test. (c) Schematic of the Seebeck measurement setup.

temperature, were monitored with an ATMOS 14 temperature and humidity sensor, and the wind speed was monitored using the METER Group weather station utilizing ATMOS 22 ultrasonic anemometers. The solar power was recorded using a MicroCache 2381 thermopile pyranometer.

The PTE behaviour of the samples was evaluated by measuring their open-circuit voltage over time. The experimental setup for conducting Seebeck measurements, as illustrated in Fig. 1c, was tailored in-house to suit the study requirements. To accurately monitor the PTE voltages of the cells, both ends of the cylindrical samples were coated with silver paint and covered with copper adhesive. The series connection was provided by using the same copper tape as an electrode and a connector. To comprehensively characterize the temperature dynamics, a customized arrangement involving p-type thermocouples connected to a Picolog datalogger and a Bosch thermal camera was used to measure the temperatures on the two sides of the copper connections. The voltage discrepancy between the two copper connections was monitored by employing a KEITHLEY 2100 6 $\frac{1}{2}$ Digit Multimeter. This multimeter, in conjunction with LabVIEW software, facilitated real-time tracking of the evolving voltage difference between the interconnected copper junctions. This carefully devised experimental configuration provided the foundation for studying the PTE response of the samples under controlled solar irradiation conditions as well as in real-world experiments.

3. Results and discussion

3.1. Proof of concept of the PTE cell design and performance

To address the limitation of vertical thermal gradients in cement-based thermoelectric (TE) systems, we developed a photothermoelectric (PTE) composite designed to generate a horizontal temperature difference. This was achieved by combining materials selected for their complementary optical and thermoelectric properties (Fig. 2a).

Key reflectance peaks reveal distinct optical responses, particularly in the visible and near-infrared (NIR) regions, highlighting the link between cement composition and optical behaviour (Fig. 2b). With lower reflectance, the black segment absorbs more solar energy, acting as the ''hot electrode''. In contrast, the white segment, with a reflectance between 0.65 and 0.87, reflects more light, minimizing absorption and functioning as the ''cold electrode''. This optical contrast is essential for maintaining a stable temperature gradient (Fig. 2c). To evaluate the potential of the cell to work as a PTE, a sample was exposed to an 850 W m^{-2} light source from a 500 W lamp. The temperature difference stabilized after 30 min (Fig. 2d), confirming the ability of the cell to sustain the gradient for PTE energy conversion.

In addition to the temperature gradient, the thermoelectric performance of the cell components is a key factor for their application in a PTE cell. The details of the TE behaviour of each segment are provided in the SI (Fig. S1). The black segment was purposely developed to achieve high thermoelectric performance, whereas the white segment was selected to function as an effective cooling material. The temperature gradient across the cell drove ionic charge carriers, mainly metal cations (Na^+, K^+) and anions (OH^-), from the hot side to the cold side.[21] This movement generates a voltage, which is analysed by monitoring the sample's open-circuit voltage throughout the experiment.

The observed voltage profile follows a characteristic trend for this material, driven by the counteracting migration of cations and anions within the pore solution (Fig. 2e). In the initial stage, cation migration dominates due to their inherently higher mobility in cementitious pore solutions. Molecular dynamics simulations by Honorio *et al.*[29] showed that under typical pore conditions, K^+ and Na^+ exhibit significantly higher diffusion coefficients than OH^-, with values ranging from 1.4–4.1 $\times$ 10^{-9} m^2 s^{-1} for K^+ and 1.3–3.8 $\times$ 10^{-9} m^2 s^{-1} for Na^+, compared to only 0.8–1.8 $\times$ 10^{-9} m^2 s^{-1} for OH^-. This difference suggests a lower effective activation energy for cation migration, supporting the initial dominance of cation-driven thermodiffusion and the observed negative PTE voltage. The Seebeck coefficient, calculated as $S = \Delta V/\Delta T$, was 0.539 mV K^{-1}, indicating peak TE efficiency. As the system heats up and the hot side exceeds 80 °C, OH^- ions gain likely sufficient thermal energy to overcome their activation barrier, consistent with a shift toward anion-dominated migration. In the second stage, this increased anion mobility counteracts the cationic flux, gradually reversing the voltage. Eventually, in the third stage, a dynamic equilibrium between ion species is established, stabilizing the voltage. The observed voltage polarity reversal at $\sim$80 °C, across different gradients and power densities, is therefore attributed to a thermally activated transition in the dominant migrating ion species.

Both the absolute temperature and the temperature gradient influence the cell voltage by affecting ion migration. Thus, irradiation power impacts the thermoelectric response by controlling heat absorption and temperature. A 9 K gradient at 450 W m^{-2} was insufficient to raise the voltage, but higher powers followed a trend similar to Fig. 2d (Fig. S2 and Table S1). Notably, at 1150 W m^{-2}, the voltage profile shifted polarity in the second stage, consistent with the black segment sample and previous research on geopolymer concrete.[24] Despite different gradients—30 K for the black sample and 18 K for the PTE cell—all samples showed a voltage sign change when the hot side reached 80 °C. This suggests that 80 °C is a threshold, enhancing anion migration by overcoming the activation energy barrier and surpassing cation effects.

Environmental factors also influence cell efficiency. A major challenge for iTE materials is leakage and evaporation, as their ionic transport medium is usually liquid or water[28,30] making them sensitive to climatic conditions like relative humidity (RH) and temperature. In cement-based iTE materials, prolonged exposure to temperatures above 50 °C reduces the thermoelectric performance. To assess rechargeability, the ability of the samples to absorb ambient humidity and regenerate PTE voltage after drying was evaluated. Contact angle measurements revealed that both PTE cell segments were highly

hydrophilic (Fig. S3a–d), facilitating moisture absorption. Rechargeability was tested by monitoring voltage profiles over three PTE test cycles. Before each cycle, the samples were oven-dried and then rehydrated in a humidity chamber, as described in the experimental section. Each drying cycle reset the PTE voltage to zero under light exposure, but rehydration restored the sample's ability to generate the same voltage (Fig. 2f). These results demonstrated the ability of the samples to recover and maintain stable TE output. To assess the environmental relevance of the recharge conditions, we analyzed the climate zones of major urban areas globally (Fig. S3e). Notably, the most populated cities—typically located in humid subtropical (Cfa), monsoon (Am), and tropical rainforest (Af) climate zones—experience nighttime relative humidity levels exceeding 50% during hot seasons, fulfilling the system's recharge requirements. In contrast, arid and desert climates with persistently low humidity are less represented among the world's most densely populated urban areas. This suggests that the proposed system is suitable for deployment in most major cities worldwide.

Connection of PTE cells (chessboard concept)

Similarly, we investigated the behaviour of the PTE system by connecting two cells in series to assess their combined voltage

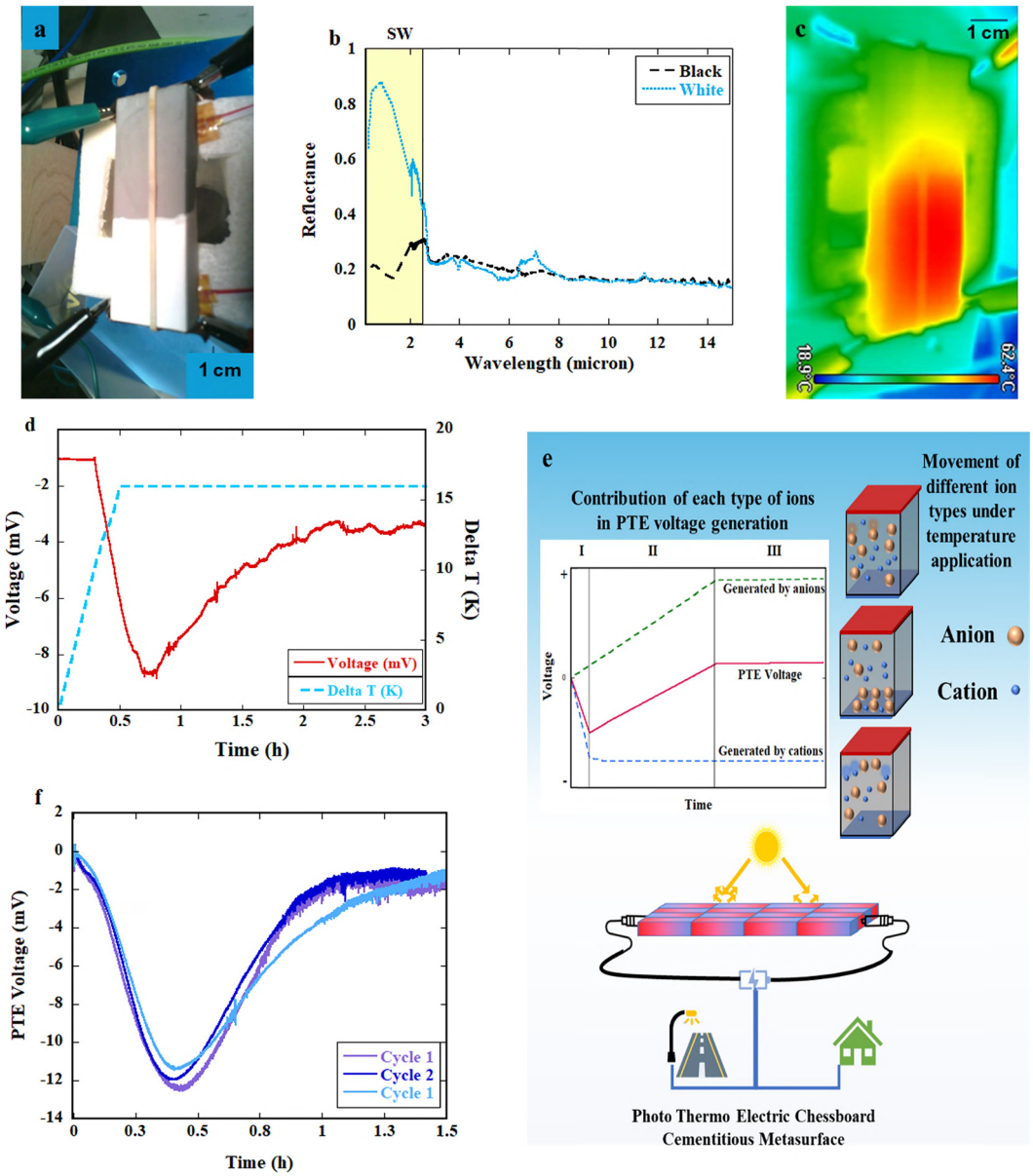

Fig. 2 (a) Digital photograph of the PTE cell prepared using two types of cement composites. (b) Light reflectance of the two parts of the PTE cell (black and white) and their difference in solar window (SW) obtained *via* FTIR spectroscopy. (c) Temperature distribution throughout the PTE cell under exposure to light at 850 W m^{-2} obtained by thermal camera after 30 minutes of illumination. (d) Temperature gradient induced in the PTE cell under 850 W m^{-2} irradiation monitored by thermocouples and the induced PTE voltage. (e) Schematic of the mechanism of the PTE cell. (f) The PTE voltage of the sample, under 950 W m^{-2} light illumination. Before each cycle the sample was dried and stored in humidity chamber at RH 50%.

response. The voltage profile under 850 W m^{-2} irradiation showed a distinct trend (Fig. 3a). During the initial stage, with a prominent negative voltage peak under similar irradiation powers, the series-connected cells generated 81% of the sum of the individual peak voltages observed in Fig. 2f. A single cell reached −8.6 mV, whereas the series configuration peaked at −13.9 mV, 3.3 mV lower than the sum of individual peaks. The series connection and sample arrangement also led to a 10% reduction in the temperature difference (Fig. 3b). Consequently, the Seebeck coefficient per cell in the series was 0.480 mV K^{-1}, which was only 11% lower than that for a single cell. Interestingly, during the second stage, the voltage decay rate was slower than that for a single cell, likely due to the reduced temperature gradient in the connected cells and reduced anion migration effect.

A decrease in TE voltage for concrete-based TE materials in series has been reported. Vareli *et al.*[15] reported a 95% decrease when 10 TE cement-based cells were connected. Our findings revealed a smaller but noticeable reduction in the peak voltage and Seebeck coefficient for PTE cells. This effect becomes more pronounced with an increasing number of cells, as confirmed by Fig. S4, where four and six PTE cells in series retained only 83% and 61% of the cumulative individual voltages, respectively. Voltage decay in large arrays is primarily an engineering issue—arising from thermal and electrical crosstalk—that can be addressed through design optimization. For instance, the system can be deployed in smaller sub-arrays connected to a central energy harvesting unit, reducing performance losses while maintaining modularity and scalability for real-world applications. Therefore, the connection of two cells is the optimal configuration for maximizing energy harvesting. Thus, a two-cell setup was selected for outdoor assessment because of its improved voltage retention and thermal gradient distribution.

Outdoor measurements (connected samples)

The performance of the developed cell under outdoor conditions was evaluated through field testing. Environmental factors such as relative humidity (RH), solar irradiance, and ambient temperature were continuously monitored to evaluate their impact on PTE cell performance (Fig. S5). Owing to the ambient RH at the test site, the samples were directly measured on the rooftop after drying to assess their rechargeability under real conditions.

As ambient humidity absorption takes time and the TE effect is primarily ionic, the TE response on the first day was minimal due to drying (Fig. S6). RH monitoring revealed an overnight increase to 95%, leading to moisture uptake (Fig. S5a). The voltage profile of the sample on the second day began shifting to negative values at 9 : 50 am (Fig. 4a) as the solar power reached 380 W m^{-2}, creating a 1 K temperature difference (Fig. 4b).

By 12 : 00 pm, it reached −52 mV at 700 W m^{-2} with a 5.5 K gradient. The voltage remained semi-constant during solar exposure, with minor oscillations due to cloud cover. On the third day (Fig. 4c), a similar correlation between solar power and TE voltage was observed, confirming the cyclability of TE energy harvesting with chessboard couples. However, the lower peak solar irradiance led to a reduced TE voltage output.

In real-world measurements, multiple parameters influence the performance of the PTE cell. In the laboratory, ambient conditions are controlled, with fixed relative humidity (RH), constant light irradiation, and no wind. In contrast, outdoor measurements are conducted under variable solar power, fluctuating RH, and wind effects. As expected, these differences result in considerable variations between the indoor and outdoor test outcomes. Outdoors, the voltage increased to 52 mV and remained stable for approximately seven hours under the peak solar power. In contrast, under artificial illumination, the negative voltage peak occurred within 30 min, followed by a gradual decrease (Fig. 3a). Additionally, the voltage under solar irradiance was approximately 3.7 times greater than that measured under equivalent irradiation power.

To elucidate the mechanism behind this difference, a detailed temperature analysis was performed. In laboratory measurements, the sample temperature under the same irradiation power reached 63 °C, about 30 °C higher than during outdoor testing. Since voltage is primarily driven by anion migration at elevated temperatures, the lower outdoor temperature minimizes anion contribution to the voltage response.

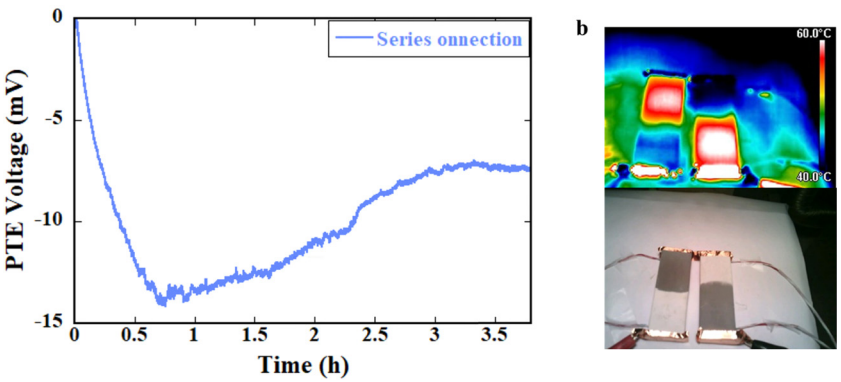

Fig. 3 (a) Voltage profile of two PTE cells connected in series under 850 W m^{-2}. (b) Temperature gradient induced in the connected system and the digital photograph of the connected cells.

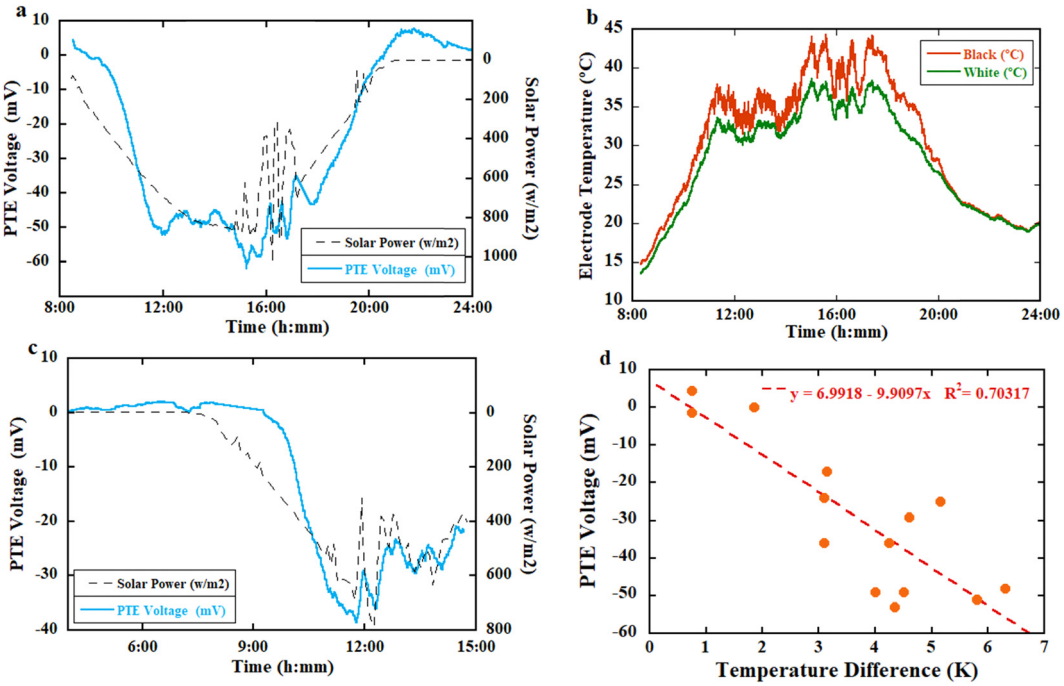

Fig. 4 (a) PTE voltage and solar power during the second day of measurement. (b) Temperature induced in each electrode. (c) PTE voltage and solar power during the third day of measurement. (d) PTE voltage *vs.* temperature difference and fit to the data for extraction of the Seebeck coefficient.

This has two effects: it prolongs the influence of cation migration and amplifies the negative voltage peak by limiting anion counteraction.

Fig. 4d shows the PTE voltage generated by two series-connected PTE cells over two days. The slope of the linear fit represents the Seebeck coefficient, calculated at 9.910 mV K^{-1}. Despite slight differences in the temperature gradient due to measurement timing and sun position, the average Seebeck coefficient per cell was 4.955 mV K^{-1}, the highest reported for cement-based TE materials. Unlike electronic TE materials, iTE materials exhibit a delay between temperature gradient formation and thermopower generation.[31] As the measurements were conducted under real conditions, weather changes such as clouds and winds caused some deviation from the linear response and resulted in an approximate value of the seebeck coefficient. These results highlight the potential of cement-based TE materials for real-world energy harvesting. Their stable voltage output under solar irradiation suggests feasibility for self-powered sensors and smart concrete structures.

PTE cells for solar energy harvesting

Measuring the open-circuit voltage and Seebeck coefficient of iTE materials provides valuable insights into their thermoelectric potential. However, these parameters alone do not fully characterize their real-world performance. When a temperature gradient is applied, ions accumulate at the electrodes, creating an electric field, making them suitable for iTE capacitors (iTECs) (Fig. 5a). When connected to an external load, electrons move to counterbalance the ionic charges, causing current flow. As a result, the measured voltage decreases under load, as ions cannot move through the external circuit. This highlights the importance of evaluating power output to assess the material's energy transfer efficiency. The instantaneous power $P(t)$ dissipated or harvested in a resistor is given by eqn (2), where $V(t)$ is the time-dependent voltage and R is the resistance. Additionally, integrating power over time (eqn (3)) provides the total harvested energy, an essential metric for applications such as self-powered sensors and energy harvesting systems.

$$P(t) = \frac{V(t)^2}{R} \quad (2)$$

$$E = \int_0^T \frac{V(t)^2}{R} \mathrm{d}t \quad (3)$$

The PTE cell voltage output was measured under 850 W m^{-2} illumination and connected to five loads ranging from 72 kΩ to 2.7 MΩ to determine the maximum power output (Fig. 5b). The maximum power output occurs when the external resistor matches the material's internal resistance. The highest power occurred when the load matched the 2.7 MΩ internal resistance, including the material and contact resistances. However, this high internal resistance limited energy harvesting to 2.81 μJ m^{-2} over five minutes under the same irradiance.

Therefore, to increase the energy output, strategies were implemented to reduce the total resistance (R), as explained in Fig. S7. These strategies include decreasing the electrode distance, improving the contact quality, and enhancing the ionic conductivity. The new samples and modifications are listed in Table 2. These changes significantly reduced the

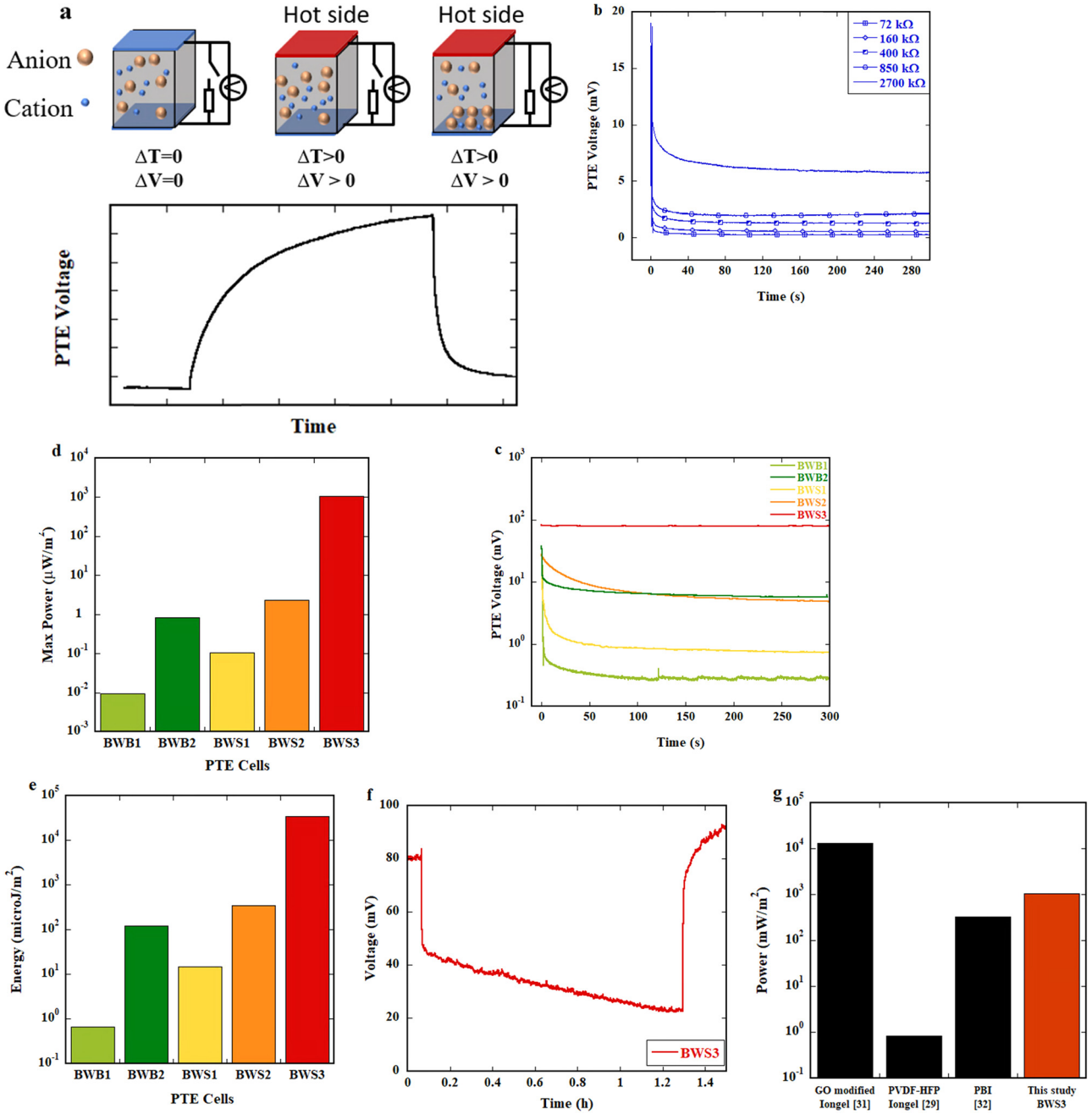

Fig. 5 (a) Working principal of an iTEC in the charging stage. (b) Voltage output of the as-produced sample connected to different external loads. (c) Voltage output of samples prepared based on different strategies (Table S2) connected to a 72 kΩ external load. (d) Energy harvested over a period of 5 minutes for each sample connected to a 72 kΩ external load. (e) Maximum power obtained for the different samples. (f) Voltage profile of the BWS3 sample connected to a 3.3 kΩ load for more than 1 h. (g) the comparison of the max power of the cement-based PTE cell with the state-of-the-art PTE materials.[30,32,33]

resistance and enhanced the conductivity, as shown in Table S2.

The PTE cells were connected to different loads to monitor their voltage output (Fig. S8) and maximum power. A 72 kΩ external load was selected for comparing the cells because the tested samples had internal resistances ranging from 2.6 kΩ to 2.7 MΩ. This load provided a suitable reference for comparing voltage outputs. The voltage of the samples under 850 W m^{-2} lamp irradiation increased as the conductivity increased (Fig. 5c). Reducing the electrode distance lowered the internal resistance by 86%, increasing energy generation per unit area 23.4-fold (Fig. 5d). A comparison of BWS1 and BWS2 revealed that the use of Ag paint electrodes increased the energy harvested by up to 56-fold. Submerged samples in NaCl solution further increased the conductivity and voltage output, leading to a higher Seebeck coefficient. This improvement is

Table 2 The different PTE cells after modifications for solar energy harvesting

Sample Name	Sample size (cm^3)	Electrode	Pretreatment after drying
BWB1	2 × 0.7 × 8	Copper tape	RH 75%
BWB2	2 × 0.7 × 8	Silver	3.5 wt% NaCl solution
BWS1	2 × 0.7 × 4	Copper tape	RH 75%
BWS2	2 × 0.7 × 4	Silver	RH 75%
BWS3	2 × 0.7 × 4	Silver	3.5 wt% NaCl solution

attributed to the substantial increase in the ion concentration induced by the seawater solution. The BWS3 sample demonstrated exceptional performance, generating 33 575 μJ m^{-2}—5.1×10^4 times higher than that of the unoptimized sample (Fig. 5e).

During the first five minutes, the PTE voltage of BWS3 remained stable at 80 mV when connected to the external load. Its high conductivity prevented significant voltage drops after connection to the resistor. This behaviour was previously reported in a perylene bisimide iTE cell.[33]

To assess performance consistency, BWS3 was connected to a 3.3 kΩ load for one hour. Fig. 5f shows the voltage output, which exhibited controlled decay but remained substantial at 25.3 mV after one hour, yielding an energy output of 1.81×10^6 μJ m^{-2}.

The optimizations significantly increased the energy harvesting potential of the PTE cells, positioning them as strong candidates for iTECs in real-world heat-to-electricity applications. Compared with state-of-the-art thermoelectric materials (Fig. 5g), this cement-based system demonstrates comparable performance while retaining the inherent advantages of cement—being inexpensive, widely available, and easy to use. By contrast, previously reported ionogel- and polymer-based devices rely on ionic liquids, graphene oxide, or high-cost specialty polymers (*e.g.*, PVDF–HFP, PBI), which require expensive feedstocks, organic solvents, and often gold electrodes, leading to material costs in the range of hundreds of dollars per square meter. In addition, these materials may present processing challenges (strict atmosphere control, hazardous solvents) and limited scalability. When benchmarked against commercial Bi_2Te_3 thermoelectric modules, which cost on the order of $$10 000–20 000 per m^2 of device area, the cement system is orders of magnitude less expensive (well below $$1 per m^2 in raw materials), albeit with lower conversion efficiency. Thus, on a cost-per-power basis, the cement approach achieves roughly $10 W^{-1}, compared to ~$40 W^{-1} for commercial Bi_2Te_3, highlighting its potential for ultra-low-cost, large-area applications where affordability and scalability outweigh peak efficiency. This combination of high efficiency and practicality makes it an attractive option for scalable and sustainable energy applications.

4. Conclusion

This study highlights the potential of PTE cementitious systems for sustainable energy conversion, demonstrating an innovative strategy that exploits the distinct light absorption properties of various cement composites. We generated controlled temperature gradients that significantly increased the energy conversion efficiency by arranging alternating black and white cement segments in a chessboard configuration. The recorded Seebeck coefficient of 9.9 mV K^{-1} for two connected PTE cells underscores the viability of using cement-based materials in low-temperature energy harvesting. Additionally, the rechargeability and cyclability of these cells under real-world conditions make them promising candidates for durable and efficient TE systems. Moreover, different strategies have been proposed to maximize the energy harvested by PTE cells, resulting in energy harvesting rates of up to 1.81×10^6 μJ m^{-2} over 1 h, which are competitive with those of the best materials in the PTE field.

Notably, industrial cement, which is a widely used, inexpensive, and accessible material, offers a unique advantage in this application. Its abundant use in construction and infrastructure, combined with its low cost and availability, positions it as a key component for advancing sustainable energy solutions. The findings of this research pave the way for further advancements in cement-based PTE materials, offering new possibilities for ambient energy harvesting in the building and civil sectors and contributing to the broader field of sustainable energy technology.

Author contributions

Conceptualization, J. S. D.; funding acquisition, J. S. D.; investigation, M. B., G. G., P. M., and J. S. D.; methodology, M. B., and G. G.; supervision, J. S. D.; writing – original draft, M. B.; writing – review and editing, M. B., G. G., P. M., and J. S. D. All authors have read and agreed to the published version of the manuscript.

Conflicts of interest

There are no conflicts to declare.

Data availability

Data underlying the results presented in this paper are not publicly available at this time but may be obtained from the authors upon reasonable request.

Supplementary information is available. See DOI: **https://doi.org/10.1039/d5mh01248a**

Acknowledgements

This work was supported by the MIRACLE project. This project has received funding from the European Union's Horizon 2020 research and innovation programme under grant agreement No 964450. We also acknowledge the grant PID2022-137845NB-C22 funded by MICIU/AEI/10.13039/501100011033, by ERDF/EU and the European Union NextGenerationEU/PRTRReferences.

References

1 X. Li, Y. Zhou, S. Yu, G. Jia, H. Li and W. Li, *Energy*, 2019, **174**, 407.
2 K. Li and B. Lin, *Renewable Sustainable Energy Rev.*, 2015, **52**, 1107.
3 M. A. Abbasi, S. Parveen, S. Khan and M. A. Kamal, *Environ. Sci. Pollut. Res.*, 2020, **27**, 18029.
4 M. Khalid, *Energy Strategy Rev.*, 2024, **51**, 101299.
5 T. Kataray, B. Nitesh, B. Yarram, S. Sinha, E. Cuce, S. Shaik, P. Vigneshwaran and A. Roy, *Sustainable Energy Technol. Assessments*, 2023, **58**, 103363.
6 X. Lu, L. Sun, P. Jiang and X. Bao, *Adv. Mater.*, 2019, **31**, 1902044.
7 J. Wang, Z. Xie and J. T. W. Yeow, *Mater. Res. Express*, 2020, **7**, 112001.
8 R. Freer, D. Ekren, T. Ghosh, K. Biswas, P. Qiu, S. Wan, L. Chen, S. Han, C. Fu, T. Zhu, A. K. M. Ashiquzzaman Shawon, A. Zevalkink, K. Imasato, G. J. Snyder, M. Ozen, K. Saglik, U. Aydemir, R. Cardoso-Gil, E. Svanidze, R. Funahashi, A. V. Powell, S. Mukherjee, S. Tippireddy, P. Vaqueiro, F. Gascoin, T. Kyratsi, P. Sauerschnig and T. Mori, *J. Phys. Energy*, 2022, **4**, 022002.
9 H. Cheng, Q. Le, Z. Liu, Q. Qian, Y. Zhao and J. Ouyang, *J. Mater. Chem. C*, 2022, **10**, 433.
10 N. Van Toan, T. T. K. Tuoi, N. Inomata, M. M. I. M. Hasnan, M. Toda, I. Voiculescu, S. M. Said and T. Ono, *Energy Convers. Manage.*, 2022, **264**, 115760.
11 H. Wang, D. Zhao, Z. U. Khan, S. Puzinas, M. P. Jonsson, M. Berggren and X. Crispin, *Adv. Electron. Mater.*, 2017, **3**, 1700013.
12 R. Moshwan, X. L. Shi, M. Zhang, Y. Yue, W. Di Liu, M. Li, L. Wang, D. Liang and Z. G. Chen, *Appl. Energy*, 2025, **380**, 125032.
13 S. Constantinou, F. Al-naemi, H. Alrashidi, T. Mallick and W. Issa, *Energy Sci. Eng.*, 2024, **12**, 1265.
14 X. Wang, S. Dong, A. Ashour and B. Han, *J. Mater. Sci.*, 2021, **56**, 16243.
15 I. Vareli, L. Tzounis, K. Tsirka, I. E. Kavvadias, K. Tsongas, M. Liebscher, A. Elenas, L. N. Gergidis, N. M. Barkoula and A. S. Paipetis, *J. Mater. Chem. C Mater.*, 2021, **9**, 14421.
16 V. P. Singh, M. Kumar, R. S. Srivastava and R. Vaish, *Mater Today Energy*, 2021, **21**, 100714.
17 T. Ji, S. Zhang, Y. He, X. Zhang and W. Li, *Adv. Mater. Sci. Eng.*, 2022, **1**, 1–11.
18 T. Ji, S. Zhang, Y. He, X. Zhang, X. Zhang and W. Li, *J. Build. Eng.*, 2021, **43**, 103190.
19 J. Wei, Y. Fan, L. Zhao, F. Xue, L. Hao and Q. Zhang, *Ceram. Int.*, 2018, **44**, 5829.
20 J. Wei, L. Zhao, Q. Zhang, Z. Nie and L. Hao, *Energy Build.*, 2018, **159**, 66.
21 Y. Wei, Y. Cui and Y. Wang, *Constr. Build. Mater.*, 2023, **364**, 129898.
22 G. Goracci, M. B. Ogundiran, M. Barzegar, A. Iturrospe, A. Arbe and J. S. Dolado, *ACS Omega*, 2024, **9**, 13728.
23 Y. Cui, Y. Wang and Y. Wei, *Fuhe Cailiao Xuebao/Acta Materiae Compositae Sinica*, 2022, **39**, 302.
24 M. Barzegar, G. Goracci, P. Martauz and J. S. Dolado, *Constr. Build. Mater.*, 2024, **411**, 134398.
25 J. Wei, Z. Nie, G. He, L. Hao, L. Zhao and Q. Zhang, *RSC Adv.*, 2014, **4**, 48128.
26 J. Wei, Y. Zhou, Y. Wang, Z. Miao, Y. Guo, H. Zhang, X. Li, Z. Wang and Z. Shi, *Energy*, 2023, **265**, 126398.
27 R. Jani, N. Holmes, R. West, K. Gaughan, X. Liu, M. Qu, E. Orisakwe, L. Stella, J. Kohanoff, H. Yin and B. Wojciechowski, *Polymers*, 2022, **14**, 2311.
28 Y. Xiong, Z. Shen, Y. Liu, J. Tong, Y. Liang and L. Xu, *Chem. Eng. J.*, 2023, **477**, 147168.
29 T. Honorio, F. Benboudjema, T. Bore, M. Ferhat and E. Vourc, *Phys. Chem. Chem. Phys.*, 2019, **21**, 11111.
30 H. Cheng, X. He, Z. Fan and J. Ouyang, *Adv. Energy Mater.*, 2019, **9**, 1901085.
31 H. Wang, U. Ail, R. Gabrielsson, M. Berggren and X. Crispin, *Adv. Energy Mater.*, 2015, **5**, 1500044.
32 S. Sun, X. L. Shi, W. Lyu, M. Hong, W. Chen, M. Li, T. Cao, B. Hu, Q. Liu and Z. G. Chen, *Adv. Funct. Mater.*, 2024, 2402823.
33 Q. Jiang, H. Sun, D. Zhao, F. Zhang, D. Hu, F. Jiao, L. Qin, V. Linseis, S. Fabiano, X. Crispin, Y. Ma and Y. Cao, *Adv. Mater.*, 2020, **32**, 2002752.